In Situ Induction of Strain in Iron Phosphide (FeP$_2$) Catalyst for Enhanced Hydroxide Adsorption and Water Oxidation

Guowei Li,* Qun Yang, Jiancun Rao, Chenguang Fu, Sz-Chian Liou, Gudrun Auffermann, Yan Sun,* and Claudia Felser*

Carbon-based materials have been widely used in heterogeneous catalysis because of their advantages of high surface area, thermal stability, and chemical inertness. However, their role in the catalysis is not fully understood although most studies conclude that the coupling between the carbon support and catalyst could reduce the charge transfer resistance and improve the kinetics of catalytic reactions such as water splitting. In this study, a carbon-modified FeP$_2$ electrocatalyst with a one-step strategy is synthesized. The tensile strain is introduced in situ in the *ab* crystal plane of the FeP$_2$ catalyst. This leads to charge redistribution between H and O atoms in the OH bonds and enhances the adsorption of reaction intermediates. In the water oxidation process, this results in a decrease in the energy barrier for the rate-determining step, specifically, the chemical step of *OH adsorption preceded by one-electron transfer. Benefiting from the optimized adsorption energy, the strained catalysts exhibit excellent oxygen evolution reaction (OER) activity with a low overpotential in addition to their increased stability. This study provides a new strategy for the introducing of strains in functional materials and provides new insights into the influence of carbon modification on OER activity.

1. Introduction

Electrocatalytic water splitting has been widely viewed as a promising alternative energy technology to avoid the problems associated with climate change and fossil fuel depletion.[1] However, the O$_2$ evolution reaction (OER) at the anode is a kinetically sluggish process related to multistep proton-coupled electron transfer.[2] Strategies within the framework of nanoengineering could significantly increase the activ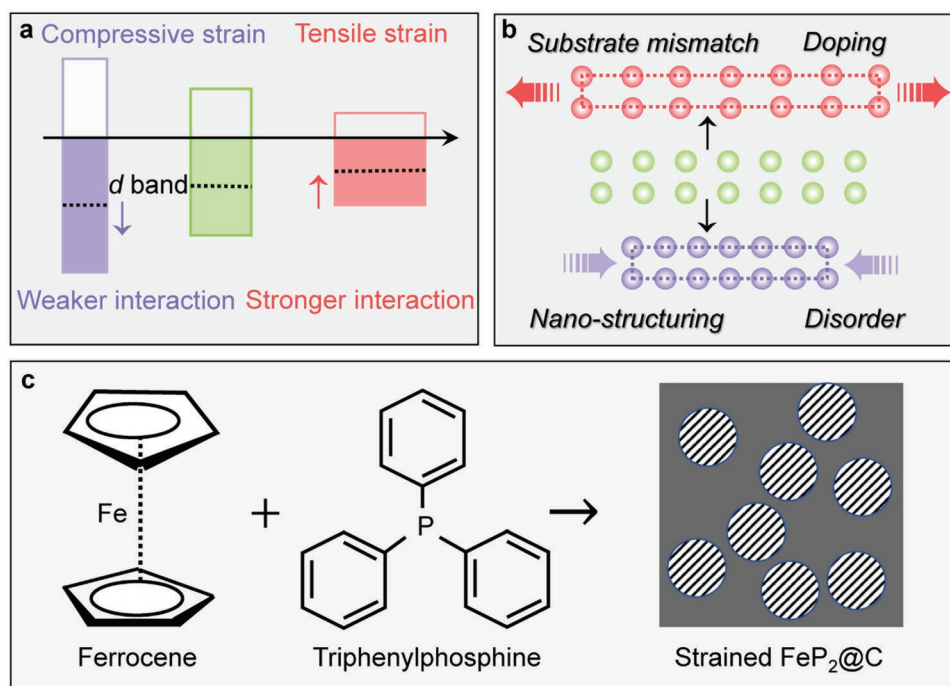ity rate by increasing the active surface area of the catalysts, thus enhancing mass and electron transport and improving electrochemical stability.[3] Incorporating carbon-based nanomaterials is an ideal solution for understanding mass transfer between the liquid electrolyte and solid catalyst surface and elucidating the kinetic reaction processes occurring on the catalyst surface.[4] Unfortunately, the complexity of the catalysts under investigation limits the understanding of the OER mechanism and catalytic processes. In addition, most theoretical treatments of the reaction routes of oxygen evolution have not considered the lattice mismatch problems between the electrocatalysts and their carbon supports. This may cause confusion about the real contributions from carbon modification and lattice mismatch.

The tailoring of lattice mismatch, or strain, at the surface of electrocatalysts, has been proven to be an effective method for regulating the electrocatalytic activities toward the OER, hydrogen evolution reaction (HER), and oxygen reduction reaction (ORR).[5] This can be explained well within the framework of the d-band model that relates adsorption energies to the d-band position. As illustrated in **Figure 1**a, in the presence of a compressive strain, the width of the d-band will increase to maintain the electron filling of d orbitals. Thus, the d-band center will shift down and away from the Fermi level, which suggests a weaker interaction with any surface adsorbates. On the contrary, a tensile strain will lead to a decrease in the d-bandwidth if no charge transfer occurs. This results in the upshifting of the d-band center toward the Fermi level and stronger interactions with surface adsorbates.[6]

Strains are generally created based on the lattice mismatch effect, which can occur after depositing the desired material onto a substrate with a different lattice parameter (Figure 1b).[7] This creates either a compressive or tensile strain localized at the interface between the desired material and the substrate. However, one can imagine that the utilization of strain effects requires reducing thin film-like catalysts down to several layers. Substitutional doping or disorder could also induce strain at the surface of the catalyst.[8] It has been reported that the presence of strain could even activate the catalytically inert planes in transition metal dichalcogenides.[9] Recent work confirms that the atomic-level control of catalyst thickness can enable the generation of strain at the surface. Activity enhancements of an

Dr. G. Li, Q. Yang, Dr. C. Fu, Dr. G. Auffermann, Dr. Y. Sun, Prof. C. Felser
Max Planck Institute for Chemical Physics of Solids
01187 Dresden, Germany
E-mail: guowei.li@cpfs.mpg.de; yan.sun@cpfs.mpg.de;
claudia.felser@cpfs.mpg.de
Dr. J. Rao, Dr. S.-C. Liou
AIM Lab
Maryland NanoCenter
University of Maryland
College Park, MD 20742, USA

Figure 1. a) Illustration of the d-band center in the presence of compressive strain or tensile strain. b) Commonly used strategies to create strain. c) Schematic illustration of the in situ synthesis of strained FeP_2 catalyst by carbon modification.

order of magnitude have been observed in 2D transition metal nanosheets.[5c] This has encouraged us to explore the question of whether we can introduce strain in situ without creating defects or using different substrates.

In this work, we report on the utilization of carbon modification to drive intrinsic strain in orthorhombic FeP_2, which is an ideal earth-abundant catalyst for water splitting. A tensile strain was observed in the *ab*-plane. We carefully investigated the reaction kinetics and found that the adsorption of reaction intermediates is the rate-determining step in the OER process. Carbon modification could increase the chemical stability and decrease the electron transfer resistance significantly. Moreover, the existence of strain could enhance the adsorption of OER intermediates and decrease the energy barrier of the rate-determining step, thus speeding up the OER process.

2. Results and Discussion

Strained FeP_2 nanocomposites were synthesized via a modified organometallic approach, as illustrated in Figure 1c. Nickel foam (NF) was immersed into N, N-dimethylformamide (DMF) solution containing ferrocene and triphenylphosphine. The NF coated with a precursor was then moved to a quartz tube furnace and heated in Ar flow. Ferrocene decomposes into iron clusters and reactive carbon and then reacts with phosphorus from triphenylphosphine to form a strained FeP_2/carbon core–shell structure (experimental details can be seen in the Supporting Information). Representative scanning electron microscopy (SEM) images at two different magnifications of the as-prepared catalyst on NF are shown in **Figure 2**a. A continuous densely packed thin layer was formed on the NF

surface, which is obviously different from the smooth surface of fresh NF (Figure S1, Supporting Information). The successful phosphorization can be verified through energy-dispersive spectroscopy (EDS, inset in Figure 1a). In the spectra, C, Fe, Ni, P, and O were observed, indicating slight surface oxidation. Transmission electron microscopy (TEM) image of the particles on the surface layer clearly confirmed the existence of nanocrystals embedded in the carbon matrix (Figure 2b). The amorphous carbon is derived from the decomposition of ferrocene as proved by the EDS analysis on the samples from different conditions (Figure S2 and Table S1, Supporting Information). The elemental mapping images obtained from energy-filtered TEM (EFTEM) imaging show that the elements Fe and P are uniformly distributed across the whole particle and decorated by carbon (inset Figure 2b). High-resolution TEM image further revealed that the nanocrystalline grains with different orientations are encapsulated by the graphitic carbon layers, as shown in Figure 2c and Figure S3 (Supporting Information). The indicated lattice fringes with a dihedral angle of ≈90.5° and spacings of about 0.17 and 0.18 nm can be readily indexed to the (211) and (12$\bar{1}$) crystal planes of the orthorhombic FeP_2 phase, respectively. To obtain the precise interplanar spacings, the selected area electron diffraction (SAED) pattern was calibrated and is shown in Figure 2d.[10] To determine the interplanar spacings precisely, the magnification of high-resolution TEM (HRTEM) images and scale bars are corrected by standard cross-grating Au sample. The interplanar spacings of the (210) and (240) facets that are parallel to the *c*-axis were increased by 2.4% and 1.5%, respectively. While for the facets perpendicular to the *c*-axis, such as (031) and (111), the interplanar spacings were decreased by ≈1%. This corresponds to a high tensile strain in the *ab*-plane of the carbon-modified FeP_2 catalyst in
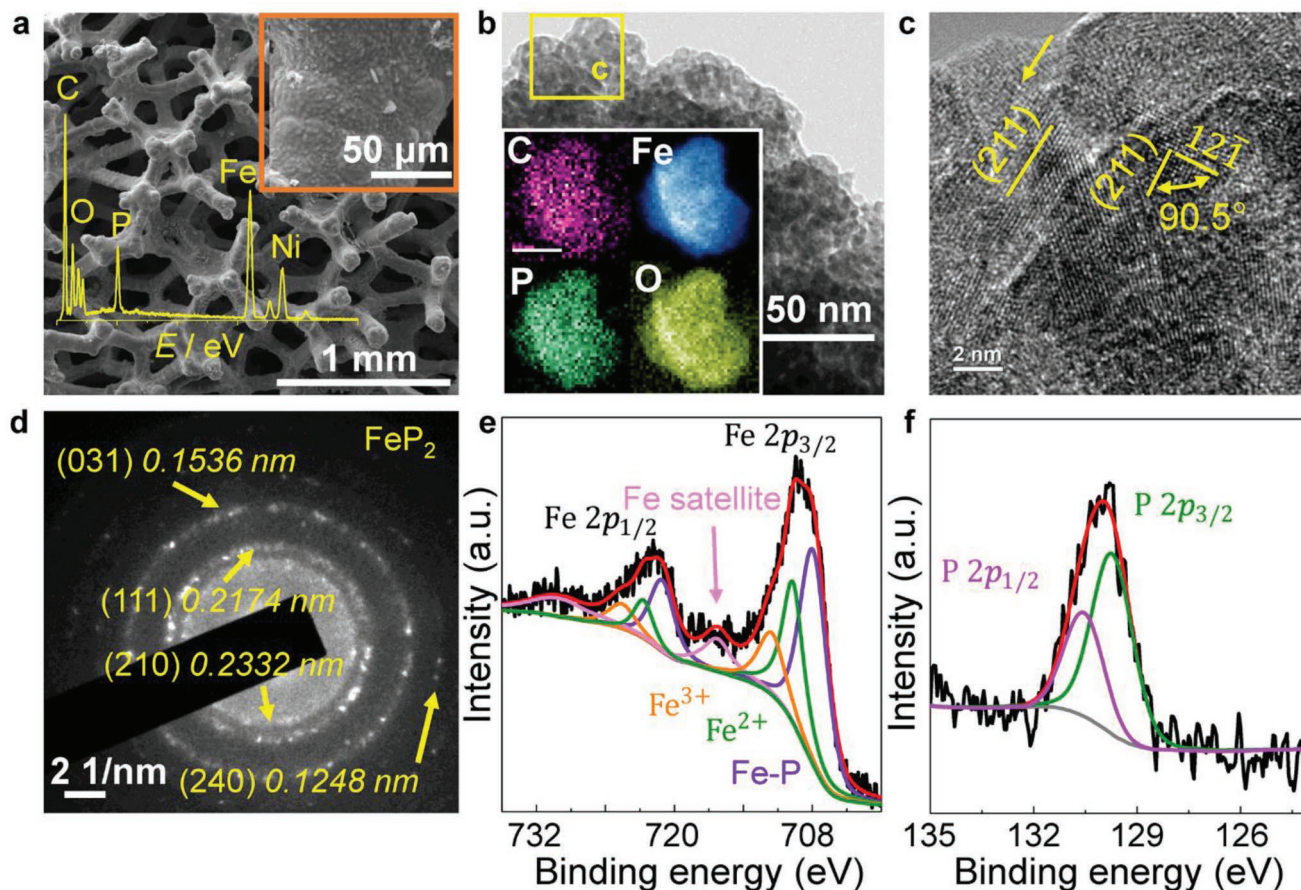
Figure 2. a) SEM image of the FeP_2 catalyst deposited on nickel foam (NF). The energy-dispersive spectroscopy (EDS) results are shown in the inset. b) TEM of the as-prepared catalysts. The elemental mapping is displayed in the inset. c,d) HRTEM and corresponding SAED pattern of the FeP_2 catalyst. e,f) High-resolution XPS spectra of Fe 2p and P 2p.

comparison with that of the pristine phase (orthorhombic FeP_2, space group *Pnnm*).[11]

The surface species and chemical states of the strained FeP_2 catalyst were investigated by X-ray photoelectron spectroscopy (XPS) (Figure S4, Supporting Information). In the high-resolution P 2p spectra (Figure 2f), the two peaks at 129.7 and 130.5 eV can be attributed to the P $2p_{2/3}$ and $2p_{1/2}$ states of the metal phosphide (FeP_2), respectively.[1b,12] The most remarkable characteristic of this spectrum is the absence of oxidized metal-phosphate species (at ≈135 eV), in contrast with reported transition metal phosphides,[13] indicating the high stability of the P-site. The Fe 2p XPS spectra suggested the existence of three chemical states on the catalyst surface (Figure 2e). The main peak with the binding energy of 707.9 eV was ascribed to Fe $2p_{3/2}$ in FeP_2.[12,14] Considering that the structure of FeP_2 can be described as Fe-centered octahedra and exhibiting diamagnetism at room temperature, we conclude that Fe takes the low-spin d^6 configuration with a valence state of 2+.[15] The higher binding energy peaks located at around 709.7 and 711.5 eV corresponding to Fe oxide species such as Fe^{2+} and Fe^{3+} resulting from the surface oxidation of strained FeP_2.[16]

The electrochemical catalytic activities of the strained catalyst for the OER were explored with a three-electrode electrochemical cell in Ar-purified 1 M KOH electrolyte. For a clear understanding of the strain effect, we also investigated the catalytic behaviors of the pure FeP_2 phase without modification or strain, NiP_2, Ni—O (NF surface was partially oxidized), and NF. As revealed in the polarization curves in **Figure 3**a, bare NF showed poor OER activity with an overpotential of 380 mV to reach a current density of 10 mA cm⁻². The pure phases of FeP_2, NiP_2, and Ni—O catalysts require lower overpotentials of 290, 280, and 257 mV, respectively, under the same conditions. They are all far inferior to the strained FeP_2 catalyst with an overpotential of only 240 mV (Table S2, Supporting Information). The Tafel slope of strained FeP_2 was calculated to be 56 mV dec⁻¹ and was much smaller than those of pristine FeP_2 (87 mV dec⁻¹), NiP_2 (136 mV dec⁻¹), Ni—O (77 mV dec⁻¹), and NF (153 mV dec⁻¹), suggesting the considerably better catalytic performance of the strained catalyst (Figure 3b). More importantly, the change in the Tafel slope also implies a change in the rate-determining step of the electrochemical reaction. A Tafel slope of ≈60 mV dec⁻¹ ($b = 2.303(RT/F)$) suggests that the OER on a strained FeP_2 catalyst may be controlled by the chemisorption of OH preceded by a facile one-electron transfer reaction.[17] A multistep chronopotentiometry curve obtained without *iR* correction is shown in Figure 3c. Upon increasing the potential, the current density changed accordingly and then
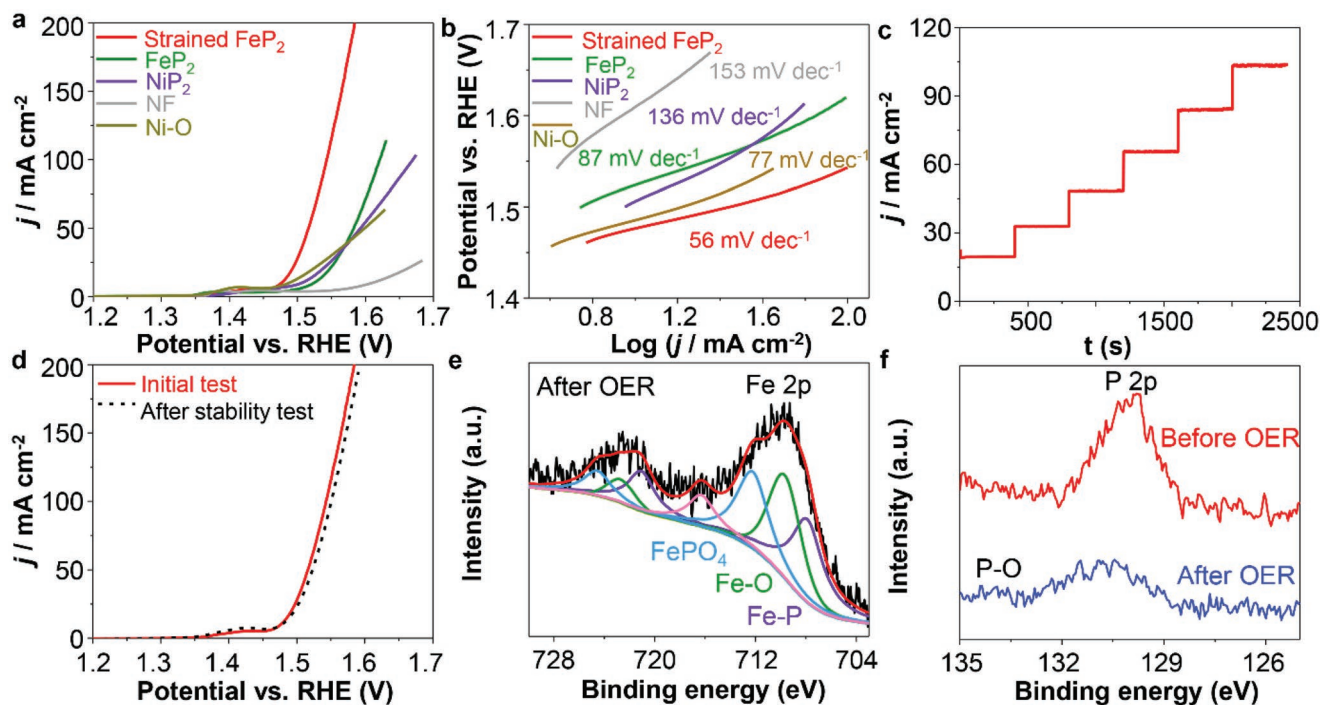
Figure 3. a) OER polarization curves of NF, NiP_2, Ni—O, pristine FeP_2, and strained FeP_2 catalysts. b) The corresponding Tafel analysis of the investigated catalysts. c) The multicurrent process with the current density increased from 20 to 105 mA cm^{-2} without *iR* correction. d) Comparison of OER polarization curves before and after stability test. e) High-resolution XPS spectra of Fe 2p after the long-time stability test. f) Comparison of high-resolution P 2p spectra before and after stability test.

stabilized quickly, suggesting the outstanding mass transfer properties of the strained FeP_2 catalyst.[18]

Stability testing of the strained FeP_2 catalyst was carried out at a high current density of 50 mA cm^{-2}. The linear sweep voltammetry (LSV) curves before and after the OER test (Figure 3d) confirmed the high durability of the catalyst in 1 M KOH solution, as only a slight decrease in current density was observed. The catalyst retained its dense structure and morphology very well without collapse after the stability test (Figure S5, Supporting Information). This was further evidenced by the similar EDS spectra (Figure S6, Supporting Information). The high-resolution Fe 2p XPS spectra revealed the existence of the Fe—P band after the long-time stability test (Figure 3e and Figure S7, Supporting Information). Partially surface oxidation may happen as evidenced by the binding energy at 712.2 eV, which can be attributed to the Fe in the $FePO_4$ phase. This can be further proved by the observation of P—O bonding from the P 2p XPS spectra (Figure 3f). The TEM image and the corresponding SAED pattern indicated that FeP_2 is still the main phase after the stability test (Figure S8a,b, Supporting Information). The interplanar spacings of the (200) facet parallel to the *c*-axis after the correction was increased by ≈1.7% and 1.5% at different positions of the catalyst surface (Figure S9a–d, Supporting Information), confirming the existence of tensile strain in the *ab*-plane after the long-time stability test. In addition, we also detected the existence of a small proportion of the $FePO_4$ phase, which is a result of surface oxidation after a long-time stability test (Figure S8c,d, Supporting Information).

To verify the influence of strain on OER activity, an understanding of the electron transfer behavior at the electrochemical interface is essential. Electrochemical impedance spectroscopy (EIS) measurements of the FeP_2 catalyst under different overpotentials are shown in **Figure 4**a. The Nyquist plots clearly reveal the presence of two semicircles, corresponding to two time constants in the OER process, which is consistent with the equivalent circuit shown in the inset of Figure 4a. In the simulation, R_Ω and CPE_{dl} represent the uncompensated solution resistance and the double-layer capacitance, while R_{CT} and R_S reflect the kinetics of the interfacial charge transfer reaction and are associated with all Faradaic steps of the OER process, rather than simply the charge transfer resistances.[19] CPE_{ad} represents the adsorption pseudocapacitance of charged surface species. The semicircle in the high-frequency regime is almost potential-independent, suggesting a fast electron transfer process. In contrast, the significant decrease in the diameter of the semicircle at low frequency with increasing overpotential corresponds to a potential-driving interfacial OER process, representing the rate-determining step. Bode plots were recorded to better distinguish these two relaxation processes (Figure 4b). The reaction time constant ($\tau = 1/\omega_p$, where τ is the time constant and ω_p is the characteristic frequency) was also calculated. It can be clearly seen that the time constant at high frequencies is much higher than that at lower frequencies. In addition, an obvious drop in relaxation time was observed in the low-frequency regime. Considering the fact that the time constant for double-layer capacitance is always higher than that for the adsorption process by several orders of magnitude, we can conclude that the OER on the strained FeP_2 catalyst is dominated by the formation of chemical intermediates, rather than the electron-transfer steps.[20] This is consistent with the observed
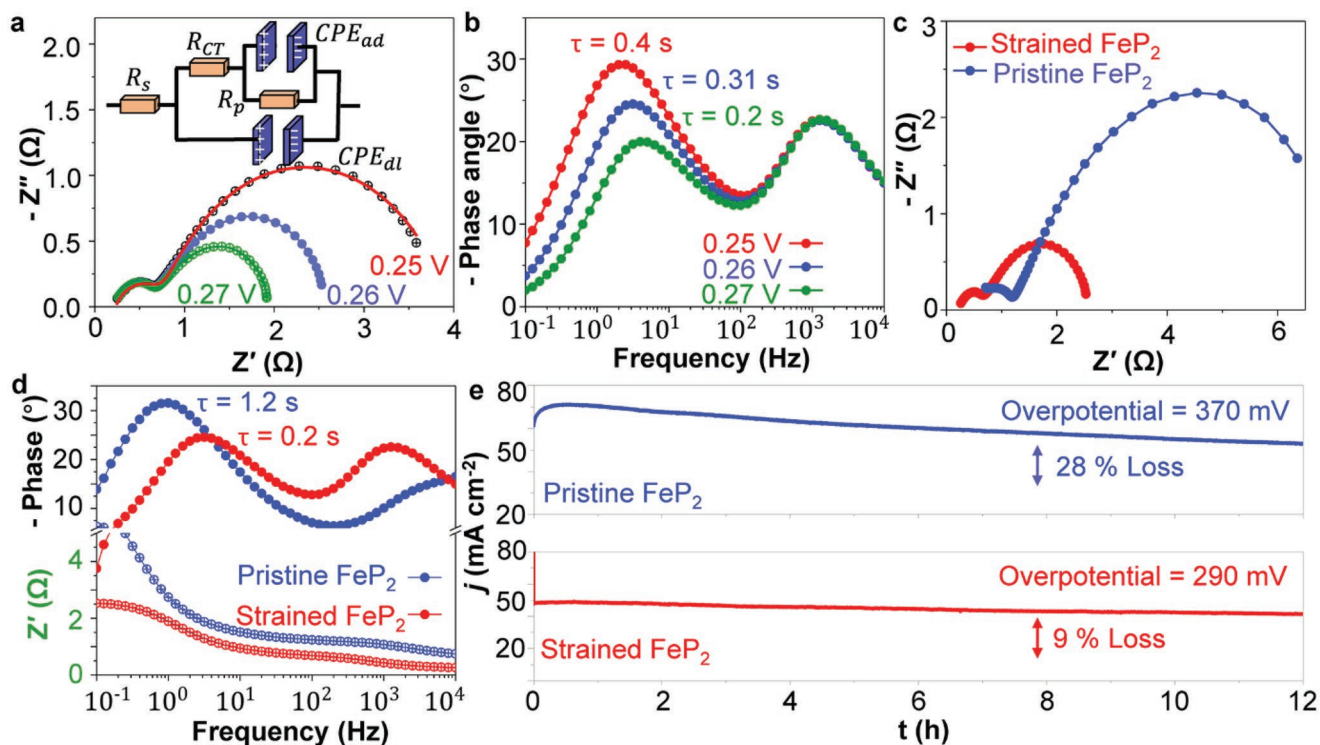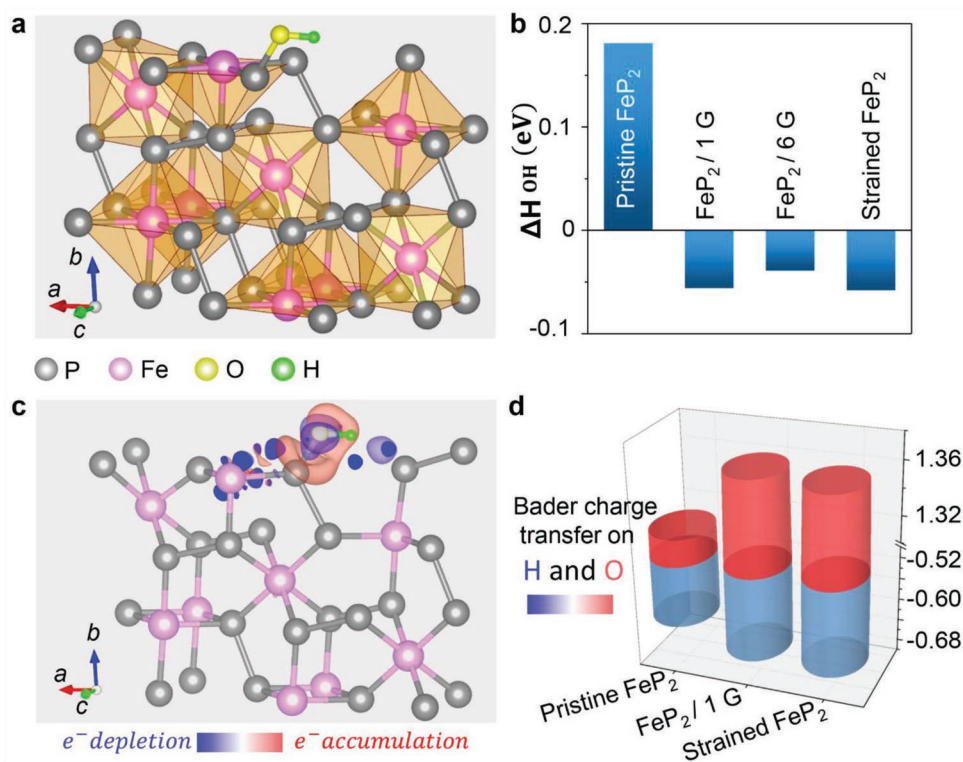
Figure 4. a) Electrochemical impedance spectra recorded in 1.0 M KOH at a series of potentials. The equivalent circuit used in the fitting is shown in the inset. b) The corresponding Bode phase diagram at different overpotentials. c) Electrochemical impedance spectra of the pristine and strained FeP$_2$ catalysts. d) The Bode format of the impedance spectra. e) Chronoamperometric responses for OER at pristine and strained FeP$_2$ electrodes in 1 and 0.1 M KOH solution.

Tafel slope of ≈60 mV dec^{-1}, further confirming that the chemical step of OH adsorption preceded by a one-electron/proton step is the rate-determining step.[17a,21]

Considering the above-mentioned analysis, we collected the EIS spectra of pristine and strained FeP$_2$ catalysts at the same overpotential (0.27 V vs RHE). As shown in Figure 4c, there was a decrease in semicircular diameters over the entire measured frequency range, more prominently at low frequencies. Bode phase plots revealed that the time constant for the adsorption process decreased from 1.2 s for the pristine catalyst to only 0.2 s for the strained one (Figure 4d). Moreover, decreases in impedance related to the charge transfer, adsorption, and solution resistance were also observed in the Bode impedance plot (lower part of Figure 4d). In addition to the fast OER kinetics, the stability was also improved after carbon modification. The chronoamperometric study indicated that at a constant overpotential, the carbon-strained catalyst exhibited a considerably slower decay than that of the pristine catalyst (Figure 4e). Thus, we can conclude here that the carbon coating not only results in increased electrochemical stability but also an enhanced adsorption process and OER kinetics as a result of the strain effect.

Theoretical and experimental investigations have all confirmed that the adsorption of oxygenated intermediates (especially *OH) is the highest-energy-consuming step in the water oxidation process. The optimization of the adsorption energy can be achieved by doping, or possibly by introducing strain.[22] Thus, density functional theory (DFT) was employed

to calculate the chemisorption free energies of *OH on the investigated catalysts. The (120) plane of orthorhombic FeP$_2$ was selected for these calculations because this plane contains both Ni and P sites simultaneously. More importantly, it was parallel to the c-axis and matches well with the graphite crystal lattice. We considered adsorption on pristine FeP$_2$, FeP$_2$ on one layer of graphene (FeP$_2$/1G), FeP$_2$ on six layers of graphene (FeP$_2$/6G), and a strained FeP$_2$ catalyst. As shown in **Figure 5**a and Figure S10 (Supporting Information), the most energetically favorable configuration for *OH adsorption was the Fe−P bridge site (closer to the P site) for all the cases. The binding energy was determined to be 0.181 eV for the pristine catalyst, suggesting weak adsorption. This is in good agreement with the Tafel and EIS analyses that showed that the chemical adsorption step is the rate-determining step. Depositing FeP$_2$ catalysts on graphite favored *OH adsorption, because the lattice mismatch between FeP$_2$ and graphite will result in a tensile strain of up to 5%. Thus, we calculated the adsorption behavior on strained FeP$_2$ without graphite support. Surprisingly, it exhibited adsorption energy of −0.058 eV, similar to that of the FeP$_2$/1G catalyst. To further explore the principle of improving the material properties by introducing strain, the differential charge distributions were calculated. As illustrated in Figure 5c and Figure S11 (Supporting Information), the charge transfer mainly occurred through the O−P bonds. Electron holes were generated around the P and Fe atoms, indicating the occurrence of charge transfer from P to adsorbed *OH. This has been definitely proven by previous research that the formation

ADVANCED
SCIENCE NEWS
www.advancedsciencenews.com

ADVANCED
FUNCTIONAL
MATERIALS
www.afm-journal.de

Figure 5. a) Optimized adsorption position for *OH intermediate on FeP_2 catalyst. b) Chemisorption free energies of *OH intermediate on the surface of pristine FeP_2, $FeP_2/1G$, $FeP_2/6G$, and strained FeP_2 catalysts. c) Charge density difference on strained FeP_2, blue represents electron depletion and red represents electron accumulation. d) Bader charge transfer analysis with the reaction *OH intermediate on pristine FeP_2, $FeP_2/1G$, and strained FeP_2 catalysts.

of reaction intermediates such as *OH requires an increase in the oxidation state at the active site during the OER process.[22c]

To better determine the contributions from the strain and graphite support, Bader charge transfer analysis was carried out. It was confirmed that the P sites are partially oxidized, losing similar amounts of electrons to the *OH adsorbate for pristine FeP_2 (0.712), $FeP_2/1G$ (0.720), and strained FeP_2 catalysts (0.713). However, both graphite support and tensile strain could lead to a redistribution of electrons between O and H in the *OH adsorbate (Figure 5d). There is an increase in the electron density around the O atoms, resulting in enhanced *OH adsorption and fast OER kinetics.

3. Conclusion

In conclusion, we present a facile route for the synthesis of strained FeP_2 electrocatalysts by graphite modification. The effects of strain and the graphite support were investigated in detail to understand the accelerated OER kinetics. We found that in addition to the decreased electron transfer resistance, the strain-induced as a result of the lattice mismatch may have caused the excellent OER activity. The tensile strain will lead to an electron distribution around the O-H bond of adsorbed *OH and enhanced reaction kinetics due to increased intermediate adsorption. This will finally decrease the energy barrier for the rate-determining step and speed up the OER process. The strategy presented here provides an effective

route to design highly efficient electrocatalysts by introducing strain in situ.

4. Experimental Section

Preparation of Strained FeP_2/C: The strained FeP_2/C catalyst was synthesized by a one-step procedure. In a typical synthesis process, a commercial Ni foam (Sigma-Aldrich, 99.5%) was cleaned ultrasonically in 1 M HCl for 10 min and then washed with ethanol and deionized (DI) water for several times. The Ni foam was put into 20 mL of dimethylformamide solution (99.8%), which contained 0.186 g ferrocene (Alfa Aesar, 99.5%) and 0.2 g triphenylphosphine (Sigma-Aldrich, 99%). The solution was maintained at 80 °C for 4 h. The Ni foam was taken out from the solution and placed into a tube furnace with Ar flow (80 mL min^{-1}). The furnace was heated to 220 °C in 30 min and then to 400 °C with a speed of 7 °C min^{-1}. Finally, the sample was maintained at this temperature for 90 min before cooled to room temperature naturally.

Preparation of Pristine FeP_2: In a typical procedure, 0.202 g iron (III) nitrate nonahydrate (Carl Roth, 99.999%) was used to replace ferrocene. All the other procedures were kept the same with the preparation of strained FeP_2 catalyst.

Preparation of Pristine NiP_2: In a typical procedure, 0.202 g nickel (II)-nitrate hexahydrate (Carl Roth, 99%) was used to replace ferrocene. All the other procedures were kept the same with the preparation of strained FeP_2 catalyst.

Preparation of Ni−O Catalyst on Ni Form: To exclude the contribution from the in situ formation of active spices at the Ni foam surface, a sample was synthesized by the reaction between Ni foam and triphenylphosphine, but without ferrocene. All the other procedures were kept the same with the preparation of strained FeP_2 catalyst.

Structure Characterization: The SEM images were obtained with a JEOL JSM 6700F electron microscope with an accelerating voltage of 5 kV. TEM, HRTEM, as well as corresponding TEM-EDS mapping were performed under an acceleration voltage of 200 kV with a TITAN 80/300 electron microscope. XPS analyses were performed using a UHV surface analysis system equipped with a Scienta-200 hemispherical analyzer. The base pressure of a sample analysis chamber is 2×10^{-10} mbar and corrected with C 1s line at 284.6 eV. The standard deviation for the binding energy values was 0.1 eV.

Electrochemical Measurements: The OER catalytic measurements were performed on an Autolab PGSTAT302N electrochemistry workstation with an impedance module. A conventional three-electrode cell configuration was used in the measurement. An Ag/AgCl (3 M KCl) electrode was used as the reference electrode, and a graphite rod was used as the counter electrode. The Ni foam with loaded electrocatalysts was attached to a Ti plate and served as a working electrode. The electrolyte was an Ar saturated 1 M KOH solution. Linear sweep voltammograms were recorded with a scan rate of 5 mV s^{-1}. The stability tests were performed at an overpotential of 290 and 370 mV for the pristine and strained FeP$_2$ catalysts. All potentials used in this work were referenced to a reverse hydrogen electrode (RHE). All the EIS experiments were performed on an Autolab model 302 N potentiostat with a frequency range from 10 kHz to 0.1 Hz and a 10 mV AC dither. Bode phase (phase angle vs frequency) and Bode modulus (impedance modulus vs frequency) diagrams are derived from the corresponding impedance spectrum.

Supporting Information

Supporting Information is available from the Wiley Online Library or from the author.

Acknowledgements

Conflict of Interest

The authors declare no conflict of interest.

Keywords

[1] a) R. Zhang, X. Wang, S. Yu, T. Wen, X. Zhu, F. Yang, X. Sun, X. Wang, W. Hu, *Adv. Mater.* **2017**, *29*, 1605502; b) I. K. Mishra, H. Zhou, J. Sun, K. Dahal, Z. Ren, R. He, S. Chen, Z. Ren, *Mater. Today Phys.* **2018**, *4*, 1; c) X. F. Lu, L. Yu, X. W. Lou, *Sci. Adv.* **2019**, *5*,

eaav6009; d) L. An, J. Feng, Y. Zhang, R. Wang, H. Liu, G.-C. Wang, F. Cheng, P. Xi, *Adv. Funct. Mater.* **2019**, *29*, 1805298.

[2] a) Z. W. Seh, J. Kibsgaard, C. F. Dickens, I. Chorkendorff, J. K. Norskov, T. F. Jaramillo, *Science* **2017**, *355*, eaad4998; b) J. Suntivich, H. A. Gasteiger, N. Yabuuchi, H. Nakanishi, J. B. Goodenough, Y. Shao-Horn, *Nat. Chem.* **2011**, *3*, 546; c) L. C. Seitz, C. F. Dickens, K. Nishio, Y. Hikita, J. Montoya, A. Doyle, C. Kirk, A. Vojvodic, H. Y. Hwang, J. K. Norskov, T. F. Jaramillo, *Science* **2016**, *353*, 1011; d) G. A. El-Nagar, M. A. Hassan, A. Fetyan, M. K. Kayarkatte, I. Lauermann, C. Roth, *Appl. Catal., B* **2017**, *214*, 137.

[3] a) T. Sun, L. Xu, Y. Yan, A. A. Zakhidov, R. H. Baughman, J. Chen, *ACS Catal.* **2016**, *6*, 1446; b) C. Bae, T. A. Ho, H. Kim, S. Lee, S. Lim, M. Kim, H. Yoo, J. M. Montero-Moreno, J. H. Park, H. Shin, *Sci. Adv.* **2017**, *3*, e1602215; c) J. Wang, L. Y. Gan, W. Y. Zhang, Y. C. Peng, H. Yu, Q. Y. Yan, X. H. Xia, X. Wang, *Sci. Adv.* **2018**, *4*, eaap7970; d) J. Hou, Y. Wu, B. Zhang, S. Cao, Z. Li, L. Sun, *Adv. Funct. Mater.* **2019**, *29*, 1808367; e) H. Zhang, X. Li, A. Hähnel, V. Naumann, C. Lin, S. Azimi, S. L. Schweizer, A. W. Maijenburg, R. B. Wehrspohn, *Adv. Funct. Mater.* **2018**, *28*, 1706847.

[4] J. Zhang, G. Chen, K. Mullen, X. Feng, *Adv. Mater.* **2018**, *30*, e1800528.

[5] a) M. Luo, S. Guo, *Nat. Rev. Mater.* **2017**, *2*, 17059; b) M. G. Sensoy, D. Vinichenko, W. Chen, C. M. Friend, E. Kaxiras, *Phys. Rev. B* **2017**, *95*, 014106; c) L. Wang, Z. Zeng, W. Gao, T. Maxson, D. Raciti, M. Giroux, X. Pan, C. Wang, J. Greeley, *Science* **2019**, *363*, 870.

[6] J. Ontaneda, R. A. Bennett, R. Grau-Crespo, *J. Phys. Chem. C* **2015**, *119*, 23436.

[7] a) Y. Wei, P. Nukala, M. Salverda, S. Matzen, H. J. Zhao, J. Momand, A. S. Everhardt, G. Agnus, G. R. Blake, P. Lecoeur, B. J. Kooi, J. Iniguez, B. Dkhil, B. Noheda, *Nat. Mater.* **2018**, *17*, 1095; b) X. He, H. Li, Z. Zhu, Z. Dai, Y. Yang, P. Yang, Q. Zhang, P. Li, U. Schwingenschlogl, X. Zhang, *Appl. Phys. Lett.* **2016**, *109*, 173105; c) D. Xu, R. Hanus, Y. Xiao, S. Wang, G. J. Snyder, Q. Hao, *Mater. Today Phys.* **2018**, *6*, 53.

[8] a) O. Kraynis, J. Timoshenko, J. Huang, H. Singh, E. Wachtel, A. I. Frenkel, I. Lubomirsky, *Inorg. Chem.* **2019**, *58*, 7527; b) A. Azcatl, X. Qin, A. Prakash, C. Zhang, L. Cheng, Q. Wang, N. Lu, M. J. Kim, J. Kim, K. Cho, R. Addou, C. L. Hinkle, J. Appenzeller, R. M. Wallace, *Nano Lett.* **2016**, *16*, 5437.

[9] H. Li, C. Tsai, A. L. Koh, L. Cai, A. W. Contryman, A. H. Fragapane, J. Zhao, H. S. Han, H. C. Manoharan, F. Abild-Pedersen, J. K. Nørskov, X. Zheng, *Nat. Mater.* **2016**, *15*, 48.

[10] C. T. Schamp, W. A. Jesser, *Ultramicroscopy* **2005**, *103*, 165.

[11] S. N. Britvin, M. N. Murashko, Y. Vapnik, Y. S. Polekhovsky, S. V. Krivovichev, O. S. Vereshchagin, N. S. Vlasenko, V. V. Shilovskikh, A. N. Zaitsev, *Phys. Chem. Miner.* **2018**, *46*, 361.

[12] J. Jiang, C. Wang, J. Zhang, W. Wang, X. Zhou, B. Pan, K. Tang, J. Zuo, Q. Yang, *J. Mater. Chem. A* **2015**, *3*, 499.

[13] a) H. Li, S. M. Xu, H. Yan, L. Yang, S. Xu, *Small* **2018**, *14*, e1800367; b) L. M. Cao, Y. W. Hu, S. F. Tang, A. Iljin, J. W. Wang, Z. M. Zhang, T. B. Lu, *Adv. Sci.* **2018**, *5*, 1800949; c) K. Liu, F. Wang, P. He, T. A. Shifa, Z. Wang, Z. Cheng, X. Zhan, J. He, *Adv. Energy Mater.* **2018**, *8*, 1703290.

[14] A. P. Grosvenor, S. D. Wik, R. G. Cavell, A. Mar, *Inorg. Chem.* **2005**, *44*, 8988.

[15] G. Boda, B. Carlsson, O. Beckman, B. Stenstrom, S. Rundqvis, V. Sagredo, *Phys. Scr.* **1971**, *4*, 132.

[16] a) G. Li, B. Zhang, T. Baluyan, J. Rao, J. Wu, A. A. Novakova, P. Rudolf, G. R. Blake, R. A. de Groot, T. T. Palstra, *Inorg. Chem.* **2016**, *55*, 12912; b) M. Li, H. Du, L. Kuai, K. Huang, Y. Xia, B. Geng, *Angew. Chem.* **2017**, *56*, 12649.

[17] a) K. Wan, J. Luo, C. Zhou, T. Zhang, J. Arbiol, X. Lu, B. W. Mao, X. Zhang, J. Fransaer, *Adv. Funct. Mater.* **2019**, *29*, 1900315;

b) Z. Chen, C. X. Kronawitter, Y.-W. Yeh, X. Yang, P. Zhao, N. Yao, B. E. Koel, *J. Mater. Chem. A* **2017**, *5*, 842.

[18] a) C. Tang, N. Cheng, Z. Pu, W. Xing, X. Sun, *Angew. Chem.* **2015**, *54*, 9351; b) W. Li, X. Gao, D. Xiong, F. Xia, J. Liu, W. G. Song, J. Xu, S. M. Thalluri, M. F. Cerqueira, X. Fu, L. Liu, *Chem. Sci.* **2017**, *8*, 2952.

[19] D. A. Harrington, B. E. Conway, *Electrochim. Acta* **1987**, *32*, 1703.

[20] a) J. O. M. Bockris, K. T. Jeng, *J. Electroanal. Chem.* **1992**, *330*, 541; b) J. R. Swierk, S. Klaus, L. Trotochaud, A. T. Bell, T. D. Tilley, *J. Phys. Chem. C* **2015**, *119*, 19022.

[21] N. T. Suen, S. F. Hung, Q. Quan, N. Zhang, Y. J. Xu, H. M. Chen, *Chem. Soc. Rev.* **2017**, *46*, 337.

[22] a) D. Zhou, S. Wang, Y. Jia, X. Xiong, H. Yang, S. Liu, J. Tang, J. Zhang, D. Liu, L. Zheng, Y. Kuang, X. Sun, B. Liu, *Angew. Chem.* **2019**, *58*, 736; b) M. Bajdich, M. Garcia-Mota, A. Vojvodic, J. K. Norskov, A. T. Bell, *J. Am. Chem. Soc.* **2013**, *135*, 13521; c) D. Friebel, M. W. Louie, M. Bajdich, K. E. Sanwald, Y. Cai, A. M. Wise, M. J. Cheng, D. Sokaras, T. C. Weng, R. Alonso-Mori, R. C. Davis, J. R. Bargar, J. K. Norskov, A. Nilsson, A. T. Bell, *J. Am. Chem. Soc.* **2015**, *137*, 1305.